Journal of Energy Storage 74 (2023) 109385

Contents lists available at ScienceDirect

Journal of Energy Storage

journal homepage: www.elsevier.com/locate/est

Research Papers

In-situ thermal reduction synthesis of porous carbon nitride doped gadolinium sulfide nanocomposite: An emerging electrode material for high-performance supercapacitor

Ponnaiah Sathish Kumar [a], Yuho Min [b], Dong Choon Hyun [c], Ji-Hyuk Choi [d,*], Sungwon Lee [e,*]

[a] Magnetics Initiative Life Care Research Center, Daegu Gyeongbuk Institute of Science & Technology (DGIST), 333 Techno Jungang-daero, Hyeonpung-myeon, Dalseong-gun, Daegu 711-873, Republic of Korea
[b] School of Materials Science and Engineering, Kyungpook National University, Daegu 41566, Republic of Korea
[c] Department of Polymer Science and Engineering, Kyungpook National University, Daegu 41566, Republic of Korea
[d] Resources & Materials Research Center, Korea Institute of Geoscience and Mineral Resources (KIGAM), Daejeon 34132, Republic of Korea
[e] Department of Physics and Chemistry, Daegu Gyeongbuk Institute of Science & Technology (DGIST), 333 Techno Jungang-daero, Hyeonpung-myeon, Dalseong-gun, Daegu 711-873, Republic of Korea

ARTICLE INFO

Keywords:
CN/Gd_2S_3 nanocomposite
Electrochemical properties
Porous electrode
Energy storage
Cycling stability

ABSTRACT

The multiple-step synthesis, harmful organic solvents, and hazardous binders are the major obstacles for supercapacitor (SC) designers. A conventional synthesis of nanocomposite is normally involves complex steps and time-consuming. To reduce these multiple steps and process time, we report carbon nitride-doped gadolinium sulfide (CN/Gd_2S_3) nanocomposite obtained via a one-step in situ thermal reduction method. In our study, we introduce poly(3,4-ethylenedioxythiophenes): polystyrene sulfonate (PEDOT–PSS) to act as a dual role of binder and conducting additive, and we use DI water as the solvent for the SC electrode. Despite the reduced fabrication steps, our electrode exhibits an extraordinary specific capacity value of 1831 F g^{-1} at 1 A g^{-1} in an aqueous 2 M KOH electrolyte, as well as 98.5 % retention after 5000 cycles. Moreover, a solid-state asymmetric SC (ASC) was further made up with activated carbon (AC) as a negative electrode and CN/Gd_2S_3 as a positive electrode, providing a high energy density of 70.95 W h kg^{-1} at a specific power density of 250 W kg^{-1} at 1 A g^{-1}. The remarkable specific capacitance retention of the ASC could maintain 86.8 % after 5000 cycles, indicating the potential application of CN/Gd_2S_3 electrode material for energy storage devices. This device (CN/Gd_2S_3//AC) showcased its practical application by powering twenty-six light-emitting diodes (LEDs) (each of 2.7 V) and appeared as an attractive energy storage unit for portable devices.

1. Introduction

For decades, supercapacitors (SCs) and batteries have been innovative energy storage devices that maintain a balance between power and demand. Among these devices, SCs outperform batteries in terms of greater power density (>10,000 W kg^{-1}), low maintenance cost, good charging stability (>10^5 cycles compared to batteries), and they also offer an affordable energy density (1–10 W h kg^{-1}) that is greater than conventional capacitors (<0.1 W h kg^{-1}). Additionally, SCs exhibit excellent circulation features, longer lifespan (>10^5 cycles), fast charge-discharge rates (within seconds), and are safe to use [1–3]. Still, the bare electrodes produce low energy density and sluggish charge and mass transfer kinetics, hindering their real applications [4,5]. Therefore, altering the electrode material is an effective factor in improving the efficiency of SCs. Carbon nitride (CN) is among the most promising electrode materials for SCs due to its two-dimensional layered structure, suitable band gap, ease of preparation, low cost, high nitrogen content and non-polluting nature [6]. In addition, the presence of nitrogen in CN itself plays an important role in improving the wetting of the electrode with the electrolyte, acting as an electron donor/acceptor, providing more active reaction sites, and inducing large additional pseudocapacitance behavior [7]. In the past, CN has been viewed as a flexible polymer that can easily be grafted onto another material. Additionally, lamellar structures with well-crystallized crystals are likely to facilitate charge transfer on the horizontal plane [8]. However, pristine CN decreases in capacitance at high current density and low surface area

* Corresponding authors.
E-mail addresses: jhchoi@kigam.re.kr (J.-H. Choi), swlee@dgist.ac.kr (S. Lee).

https://doi.org/10.1016/j.est.2023.109385
Received 5 June 2023; Received in revised form 25 September 2023; Accepted 20 October 2023
Available online 31 October 2023

[7]. Hence, a lot of researchers have been focused on increasing the surface area, electrochemical capacitance, and energy density of CN by introducing pseudocapacitance through the combination with metal sulfides [9]. Interestingly, gadolinium sulfide (Gd_2S_3) is widely used in electronic imaging and biological research, fuel cells, semiconductor technology, photoluminescence studies, energy storage applications, and electrocatalysis [10,11]. In Gd^{3+}, it can improve the electrical conductivity of the resulting solid electrolyte, which is ideal for supercapacitors and energy storage applications [12]. For instance, V. Mariyappan et al. also reported Gd_2S_3 rod-embedded RGO for highly selective electrochemical sensing of carbofuran [13]. K.Y. Kumar et al. reported on Gd_2S_3-anchored nitrogen-doped RGO for electrochemical detection and photodegradation of carbendazim [14]. Based on the previous reports, we have investigated the combination of Gd_2S_3 with carbon-based composite materials to improve the conductivity, surface area, porosities, electrocatalytic activity, and cyclic stability. To produce metal sulfide-doped CN, various methods have been employed, each with its own disadvantages. These include the use of excess chemicals, which could have adverse effects on the environment and living organisms, the requirement of multiple synthetic steps, and the lengthy duration of the process [15]. Therefore, a simple method is needed for large-scale production. Our study demonstrates a one-pot thermal reduction synthesis of a CN/Gd_2S_3 nanocomposite derived from dicyandiamide (as a CN source), $Gd(CH_3CO_2)_3$ (as a Gd^{3+} source), and thioacetamide (as a sulfide source), followed by simple grinding and pyrolysis. The grinding process ensured a homogeneous mixture of the precursors, which is essential for the subsequent reaction. The pyrolysis, conducted in a confined environment under high-temperature conditions, produced an amorphous form that subsequently began to crystallize and enhance porosity. Due to its chemical strength, Gd^{3+} physically interacted with C_2H_5NS (a sulfur source) during the grinding method. The final mixture obtained was pyrolyzed in a closed crucible. During the heating process, the decomposition of C_2H_5NS and the release of sulfur, which then reacted with the metal ions from Gd $(CH_3CO_2)_3$ to form Gd_2S_3. In general, fluorine-containing polymers, such as polytetrafluoroethylene (PTFE) and polyvinylidene fluoride (PVDF), are the most widely used binders in SC electrodes. However, these binders are electrically insulating, requiring conductive additives, and they must be dissolved in toxic organic solvents such as *N*,*N*-dimethylformamide (N,N-DMF) and *N*-methyl-2-pyrrolidone (NMP) during the electrode fabrication process [16–18]. Furthermore, these binders block the available surface area of active materials, decreasing the capacitance of the SC electrodes [19,20]. Instead, the PEDOT:PSS binder disintegrates in a water stream, allowing EDLCs with coated electrodes to be recycled using proposed protocols based on liquid processing and separation methods [17]. In this study, we introduce a one-step in-situ thermal reduction synthesis of porous CN/Gd_2S_3. The key to the success of reducing fabrication steps is the application of poly (3,4-ethylenedioxythiophenes): polystyrene sulfonate (PEDOT:PSS), which acts as both a binder and a conducting additive, along with DI water as the solvent for SC electrode preparation. Despite the reduced synthesis steps and the use of PEDOT:PSS with DI water, the fabrication process is effective. Our designed electrode exhibits enhanced specific capacitance (1831 F g^{-1} at 1.0 A g^{-1}) and high stability (98.5 % after 5000 cycles at 6.0 A g^{-1}), which is ascribed to the synergistic effect between CN/Gd_2S_3 and PEDOT:PSS. More notably, our asymmetric SC device CN/Gd_2S_3//AC delivers an excellent specific capacitance of 157.6 F g^{-1} and an energy density of 70.95 W h kg^{-1} at a power density of 0.250 kW kg^{-1}, while also displaying exceptional cycling stability at 8.0 A g^{-1} for up to 5000 consecutive cycles without discernible capacitance fading. Based on these results, we conclude that CN/Gd_2S_3 electrodes provide a simple way to fabricate large-scale all-solid-state electrodes as high-performance SCs for energy storage applications.

2. Experimental section

2.1. Materials

Gadolinium(III) acetate ($Gd(CH_3CO_2)_3{\cdot}4H_2O$), thioacetamide ($C_2H_5NS$), dicyandiamide ($C_2H_4N_4$), poly(3,4-ethylenedioxythiphoenes): polystyrene sulfonate (PEDOT–PSS) and Ni foam (NF) were purchased from Sigma-Aldrich. A Millipore water system was used to obtain deionized (DI) water, which was used throughout the experiment.

2.2. Preparation of CN/Gd_2S_3

In a typical procedure, $Gd(CH_3CO_2)_3{\cdot}4H_2O$ (0.6 g), C_2H_5NS (1.2 g) and $C_2H_4N_4$ (1.0 g) were thoroughly ground using a mortar and pestle until a homogeneous mixture was obtained. The improvement of this combination method is that it occurs in the solid state devoid of adding any solvent. Then the above mixture was heated at 200 °C for 1 h at a heating rate of 3 °C min^{-1} in the closed crucible. The cleavage of the $(CH_3CO_2)_3$ group exposes Gd atoms (unoccupied orbitals), which significantly promotes the chemisorption of electronegative sulfide ions and forms the high binding energy Gd—S bond. The presence of $C_2H_4N_4$ in the above mixture was continued at 520 °C for 4 h to produce the CN/Gd_2S_3 nanocomposite. Finally, the above mixture was cooled to room temperature. The formation of the CN/Gd_2S_3 nanocomposite was washed five times by centrifugation using DI water and ethanol and further dried at 60 °C overnight in a vacuum. The advantages (one-step formation, absence of solvents, less time-consuming and water-soluble binder) of our synthesis method are summarized in Table S1 in the Electronic supplementary materials (ESM).

2.3. Electrode preparation for SC

Then, blank Ni foam (NF) (1 cm × 1 cm) was pretreated with 5 % HCl and immersed in a transparent reaction solution at 140 °C for 2 h. Subsequently, the NF was washed three times with water and ethanol and then dried at 60 °C for 4 h. The obtained NF was coated with a slurry containing 80 % by weight of CN and CN/Gd_2S_3, and 20 % by weight of PEDOT:PSS, in two drops of deionized water (DI). It was then dried at room temperature for 6 h. In this study, a water-soluble PEDOT:PSS binder was used for the supercapacitor (SC) as it exhibits high conductivity and, when coated on a current collector, provides numerous active locations for chemical reactions [17]. The materials used, including bare NF, CN/NF, and CN/Gd_2S_3/NF, served as working electrodes, while a platinum wire was used as the auxiliary electrode, and an Ag/AgCl (saturated KCl) electrode was used as the reference electrode. The electrolyte used was 2.0 M KOH, which is safer to operate and offers greater ionic conductivity (>100 mS cm^{-1}) for the SC study. Electrochemical impedance spectroscopy (EIS) was conducted using a multichannel potentiostat (Biologic, VSP) in the frequency range of 0.1 Hz to 100 kHz. Various electrochemical characterization methods, including cyclic voltammetry (CV) and galvanostatic charge-discharge (GCD) techniques, were performed using an AUTOLAB PGSTAT302F. The CV was carried out at several scan rates (3 to 31 mV/s) within the potential range of 0 to 0.7 V.

2.4. Two-electrode asymmetric cell

The hybrid supercapacitor was assembled using AC-coated NF as the negative electrode and CN/Gd_2S_3-coated NF as the positive electrode. The mass loading of the electrodes was adjusted using the charge-mass balanced relationship as follows (Eq. (1)) [4]:

$$m+/m- = C-V-/C+V+ \quad (1)$$

where m+ and m− represent the masses, C+ and C− indicate the capacitance, and V+ and V− refer to the potential windows of the

positive and negative electrodes, respectively. The estimated specific capacities of CN/Gd_2S_3 and AC are 1831 F g^{-1} and 68 F g^{-1}, respectively, at a current density of 1 A g^{-1}. The individual voltage windows of CN/Gd_2S_3 and AC are 0.5 V and 1.0 V, respectively. Consequently, to fabricate the hybrid device, a mass ratio of approximately 0.1:1.35 between CN/Gd_2S_3 and AC was maintained. The mass loading of CN/Gd_2S_3 and AC is approximately 0.1 mg (2 mg cm^2) and 1.35 mg (27 mg cm^2), respectively. The AC electrode was fabricated by coating slurries onto NF, where the slurries were obtained by mixing AC (80 % by weight) and PEDOT:PSS (20 % by weight) in two drops of deionized water (DI) and dried at room temperature for 6 h. Next, a two-electrode configuration was constructed using the synthesized polymer gel directly, and the device, including the electrodes and separator, was separated with a 1 mm cellulose paper. For the continuous stirring method, 6.0 g of PVA was mixed with 40 mL of water, and the mixture was heated for 2 h at 85 °C to form a clear solution. Then, 3.0 g of KOH dissolved in 20 mL of DI water was added drop-wise to the clear polymer solution, resulting in the formation of a composite gel of PVA and KOH.

2.5. Physical characterization

The molecular stretching of the samples was examined by Fourier transform infrared (FT-IR) spectroscopy using a Thermo Scientific/Nicolet Continuum instrument. Powder X-ray diffraction patterns were obtained using a Rigaku diffractometer (Miniflex 600) at a scan rate of 2° min^{-1} with Cu-Kα radiation (λ = 1.5406 Å) in the 10–70 degree range. Scanning electron microscopy (SEM) images of the materials were obtained using ultra-high-resolution scanning electron microscopy (UHR-FE-SEM, Hitachi/SU8230). The Ultrahigh-Resolution and Field Emission transmission electron microscopy, elemental mapping, selected area diffraction, and energy-dispersive X-ray spectroscopy (EDAX) were performed on a UHR-TEM (Themis Z) & FETEM (Hitachi/HF-3300). X-ray photoelectron spectroscopy (XPS) was conducted to confirm the chemical states of the elements using a Thermo Scientific/ESCALAB 250Xi. The Brunauer-Emmett-Teller (BET) and Barrett-Joyner-Halenda (BJH) experiment was conducted using Quantachrome (Quadrasorb evo). Before adsorption-desorption measurements, the prepared sample was subjected to degassing at 200 °C for 5 h using

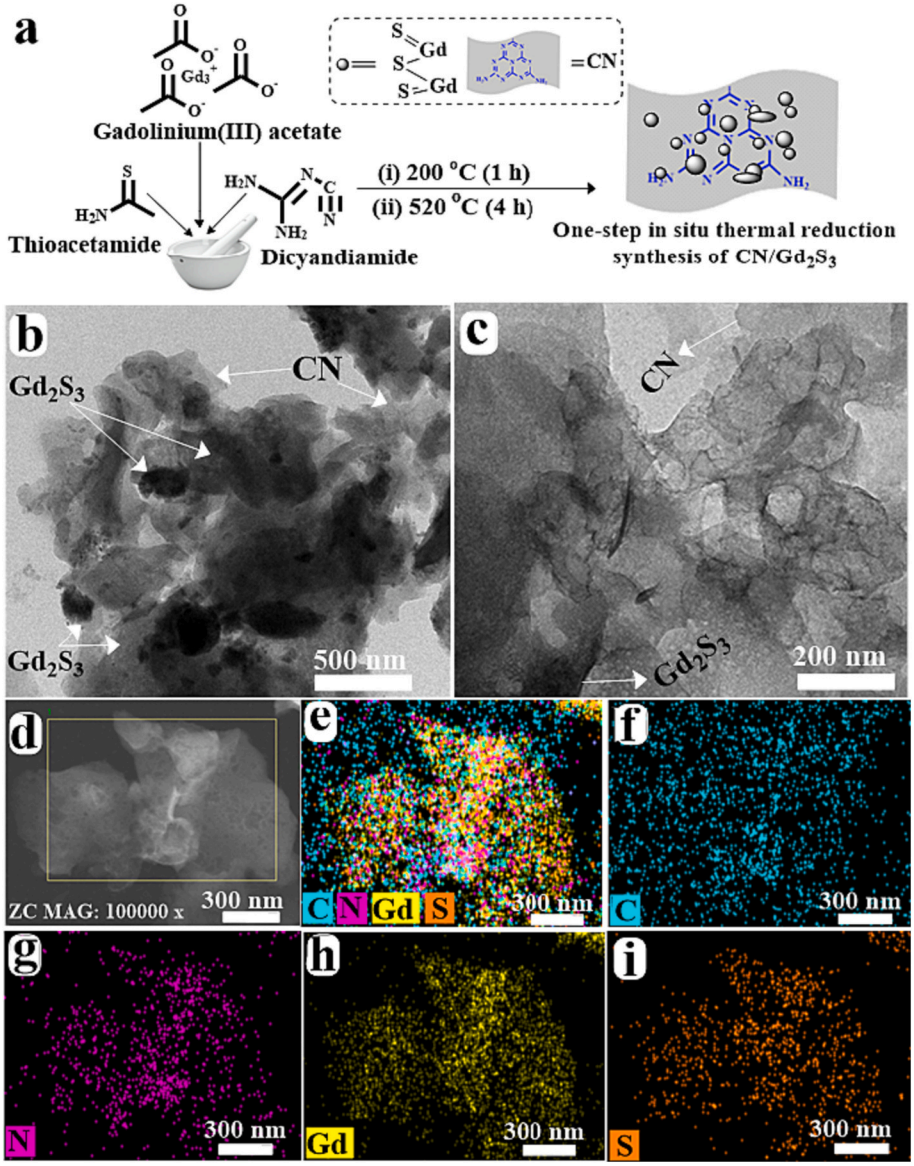

Fig. 1. Pictorial illustration of the preparations of the CN/Gd_2S_3 nanocomposite (a), different magnification FE-TEM images of the CN/Gd_2S_3 nanocomposite (b–c), FE-TEM elemental mapping of the selected area (d), elemental mapping analysis of the CN/Gd_2S_3 nanocomposite (e), including carbon map (f), nitrogen map (g), gadolinium map (h) and sulfide map (i).

nitrogen gas.

3. Results and discussion

In the typical experimental procedure, the mentioned amounts of the solid precursors, $Gd(CH_3CO_2)_3$ and C_2H_5NS, were transferred into the mortar and ground using a pestle. Due to its chemical reactivity, $Gd^{(III)+}$ physically interacted with C_2H_5NS through the grinding method. Then, $C_2H_4N_4$ was added to the mixture and ground until a homogeneous mixture was obtained. The final mixture obtained was pyrolyzed at 520 °C for 4 h in a closed crucible. During the thermal decomposition process, C_2H_5NS decomposed, converting $Gd^{(III)+}$ to Gd_2S_3 and $C_2H_4N_4$ to CN. Additionally, CO and CO_2 were evaporated from the precursor mixture, forming a porous structure in the CN/Gd_2S_3 nanocomposite. Therefore, the synthesis of the CN/Gd_2S_3 nanocomposite and the regulation of the pore structure were performed in one step (Fig. 1a). The discussion below clearly explains the detailed physicochemical properties and morphology of the synthesized nanocomposite.

The FT-IR examination was conducted to analyze the intermolecular stretching and functional groups present in the pristine CN and CN/Gd_2S_3 nanocomposite, as shown in Fig. S1a. Curve a represents the FT-IR spectrum of CN, where peak formations occur at 3010–3520 cm^{-1} due to N—H stretching vibrations. Peaks appearing in the range of 1624–1220 cm^{-1} are associated with C—N heterocyclic stretching modes, while peaks at 800–882 cm^{-1} are related to triazine unit bending vibrations [21]. On the other hand, curve b displays the FT-IR spectrum of the CN/Gd_2S_3 nanocomposite, showing a solid peak at 623 cm^{-1}, which is ascribed to the Gd—S bond [13]. As all peak intensities of the nanocomposite shifted to higher wavenumbers compared to CN, it is specified that Gd_2S_3 is adsorbed onto the surface of CN via electrostatic interactions, π–π stacking, or hydrogen bonding [14]. This result confirms the embedding of Gd_2S_3 on CN in the CN/Gd_2S_3 nanocomposite. The XRD examination was conducted to analyze the crystalline nature of CN and CN/Gd_2S_3 samples, as shown in Fig. S1b. Clear characteristic peaks for CN (curve a) at 13.1°, 26.9°, 44.3°, and 55.8° were well indexed to reflections of (100), (002), (201), and (004) planes, respectively [22]. The sharp diffraction peaks at 2θ = 16.4°, 22.9°, 24.3°, 26.9°, 30.9°, 34.2°, 35.9°, 37.9°, 38.6°, 38.8°, 42.3°, 43.6°, 44.6°, 46.4°, 47.9°, 50.4°, 51.6°, 54.1°, 57.8°, 60.8°, 61.9°, 63.5°, and 66.4° were indexed to the (200), (202), (011), (103), (302), (013), (113), (204), (312), (213), (114), (105), (214), (020), (314), (305), (512), (321), (611), (701), (224), (316), and (017) crystalline lattice planes of the CN/Gd_2S_3 nanocomposite as shown in curve b. The XRD patterns of the Gd—S with Gd to S ratios of 1:1, 1:2 and 1:3 are provided in Fig. S1c in the ESM. High conductivity is expected if the electrode material is highly crystalline; hence, the results indicate that the CN/Gd_2S_3 nanocomposite is more crystalline. Furthermore, this obtained CN/Gd_2S_3 had an orthorhombic structure with cell parameters of a = 10.74 Å, b = 3.89 Å, and c = 10.54 Å, which are well-matched to their standard JCPDS no. 43–1351. Notably, no additional peaks appear in CN/Gd_2S_3 composite, revealing that Gd_2S_3 is ingrained in the CN matrix. The average crystalline size of CN/Gd_2S_3 was determined to be 63 ± 2 nm using the Debye-Scherrer equation [23].

The morphology, elements present, and crystallinity of the synthesized samples (CN and CN/Gd_2S_3) were thoroughly investigated using UHR-FE-SEM, EDX, FE-TEM, SAED, and Mapping analysis. In the UHR-FE-SEM images of pristine CN (Fig. S2a–c) displays irregular multilayered nanosheets were observed, making it a suitable substrate [8]. In Fig. S2d–f, the CN/Gd_2S_3 images reveal that Gd_2S_3 is dispersed on the CN surface, indicating that the developed nanocomposite still retains its structural presence due to its moderate stability and strong interactions at the interface. Furthermore, the particle size and structural information were confirmed from FE-TEM images. Fig. 1b–c shows Gd_2S_3 particles continuously loaded on the smooth surface of CN, with an average size of 80–95 nm. We expect that the interaction between Gd_2S_3 and CN will lead to a significant improvement in electrochemical properties [6]. Moreover, high-resolution FE-TEM images in Fig. S3a–c clearly show the higher porosity of the CN/Gd_2S_3 nanocomposite. The achieved porous surface properties of CN/Gd_2S_3 ensure access of OH^- ions from the electrolyte to the active electrode material, enhancing the diffusion rate of redox reactions and directly improving capacitive performance [24]. Additionally, crystallized rings were observed in the SAED pattern in Fig. S3d. According to the EDX analysis (Fig. S3e), the CN/Gd_2S_3 nanocomposite contains C, N, Gd, and S. Fig. S3f displays the weight percentages (39.59, 6.66, 51.12, and 2.63) and atomic percentages (78.88, 11.38, 7.78, and 1.96) of C, N, Gd, and S elements in the CN/Gd_2S_3 nanocomposite, respectively. Fig. 1d shows the selected mapping area, demonstrating the close link between Gd_2S_3 and CN nanosheet. The HR-TEM analysis and relevant discussion of the CN/Gd_2S_3 nanocomposite are provided in Fig. S4a–c in the ESM.

FE-TEM overall elemental mapping examination (Fig. 1e) was also conducted on the CN/Gd_2S_3 nanocomposite, which shows the consistent distribution of C, N, Gd, and S species (Fig. 1f–i). The elements were found to be homogeneously distributed, leading us to conclude that Gd_2S_3 is ingrained within the CN nanostructure.

The XPS scan signals were used to examine the chemical composition and surface oxidation state of the CN/Gd_2S_3 nanocomposite. In the survey scanning spectrum (Fig. 2a), signals for C, N, Gd, and S can be seen, confirming the formation of the composite with additional evidence. The high-resolution spectrum of C 1s (Fig. 2b) reveals three deconvoluted peaks at 284.70, 286.51, and 288.86 eV, representing the C–C/C=C, C-NH, and N-C=N groups, respectively [25]. The N 1s spectrum of CN/Gd_2S_3 (Fig. 2c) shows dominant signals for triazine rings (398.5 eV), tertiary nitrogen groups (399.9 eV), and amino functions (400.7 eV) [26]. In the high-resolution Gd 4d binding energies (Fig. 2d), two major peaks appear at binding energies of 143.9 eV and 148.8 eV, corresponding to the Gd $4d_{5/2}$ and Gd $4d_{3/2}$ states, respectively, indicating the presence of Gd^{+3} oxidation state, consistent with previous literature findings [13]. The S 2p XPS spectrum is exhibited in Fig. 2e, with two major peaks at 169.6 eV and 164.1 eV for S $2p_{1/2}$ and S $2p_{3/2}$ electronic states, respectively [14]. The results indicate that the CN/Gd_2S_3 nanocomposite possesses nitrogen atoms in carbon and sulfide atom-attached Gd, which not only contributes to pseudo capacitance but also increases electrical conductivity, wettability, and boosts capacitance activity. These characteristics are beneficial in achieving excellent capacitive performance [27]. As SC energy storage involves the reversible adsorption of electrolyte ions into electrode pores, increasing the number of pores to accommodate the ions is the most desirable way to improve charge storage [28]. In this regard, the surface area pore and diameter size distribution of CN and CN/Gd_2S_3 samples were determined using Barrett-Joyner-Halenda (BJH) and N_2 adsorption/desorption isotherms, as displayed in Fig. 2f. High-specific surface area and pore diameter size are crucial to enhance the capacitive performance of electrode materials [29]. The specific surface area of the synthesized CN was found to be 12.84 $m^2\ g^{-1}$ with a pore diameter size of 3.05 nm, as shown in Curve (a). On the other hand, the CN/Gd_2S_3 nanocomposite exhibited a specific surface area of 14.13 $m^2\ g^{-1}$ with a slightly larger pore diameter size of 3.82 nm, as shown in Curve (b). Therefore, it can be expected that CN/Gd_2S_3 provides a higher surface area and pore diameter size, leading to a significant improvement in the interaction area between the electrolyte and electrode. This enhancement is important for improving capacitance performance and sustaining structural stability during fast electrochemical reactions.

4. Electrochemical behavior of CN/Gd_2S_3 toward SC applications

The performance of the device, in terms of power and energy density, capacitance, rate performance, cyclability, and safety, depends on the electrolyte used. In general, aqueous electrolytes exhibit at least several orders of magnitude higher conductivity than ionic liquids and organic electrolytes, and they can be easily manipulated in the laboratory

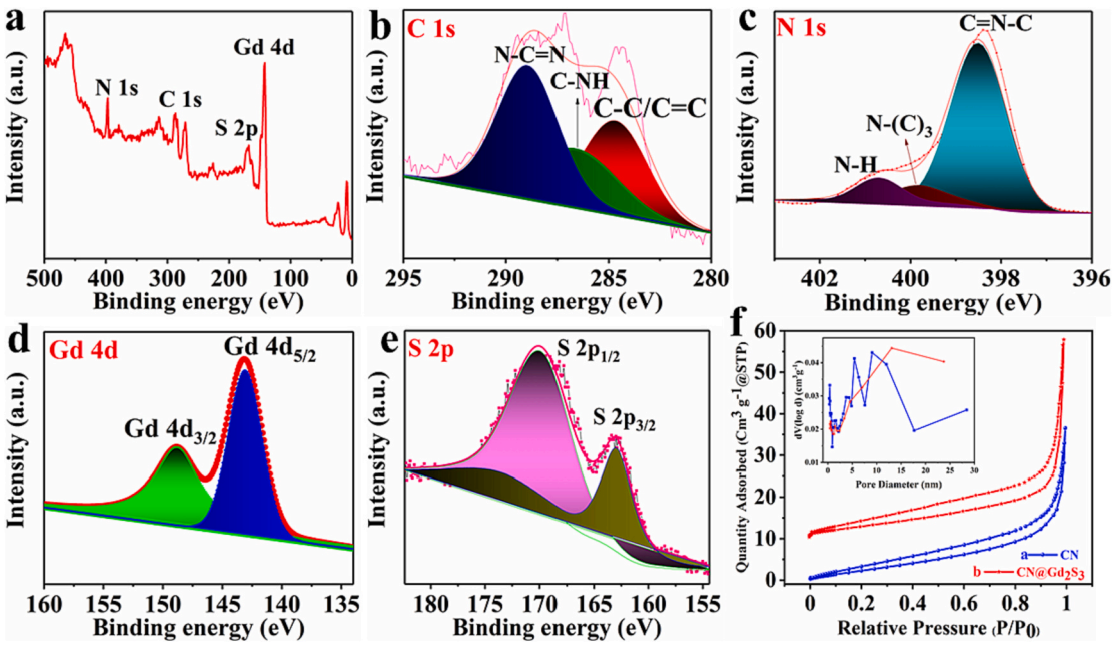

Fig. 2. XPS investigation spectrum of the CN/Gd_2S_3 nanocomposite (a), high-resolution XPS investigation spectrum of C 1s (b), N 1s (c), Gd 4d (d) and nitrogen adsorption-desorption isotherms of the CN/Gd_2S_3 nanocomposite (inset pore size distribution curve) (f).

without unusual conditions, greatly facilitating the manufacturing and assembly process [30]. Among aqueous electrolytes, KOH is low cost, low toxicity, easily available at high purity, and has high conductivity and mobility in aqueous solution [31]. The electrochemical interfacial properties of the electrode mainly depend on the capacitive double layer (C_{dl}), charge transfer resistance (R_{ct}), Warburg impedance (Z_w), and electrolyte resistance (R_s). It is well known that the diameter of the semicircular curve of the Nyquist plot is directly proportional to the resistance (R_{ct}) and is the key parameter governing the specific power of the SC [8]. In this regard, the electrochemical performances of bare NF (black curve), CN/NF (blue curve), and CN/Gd_2S_3/NF (red curve) of SC electrodes were evaluated in a three-electrode cell with an applied frequency range of 0.1 Hz to 100 kHz using EIS technique in 2 M KOH electrolyte, as shown in Fig. 3a. From these results, the Nyquist plot of CN/Gd_2S_3@NF displays a semicircle with a small diameter, which indicates a short diffusion time, high conductivity, and fast electron transfer in the electrochemical process [32]. This result suggests that CN/Gd_2S_3 has better ion diffusion and lower charge transfer resistance

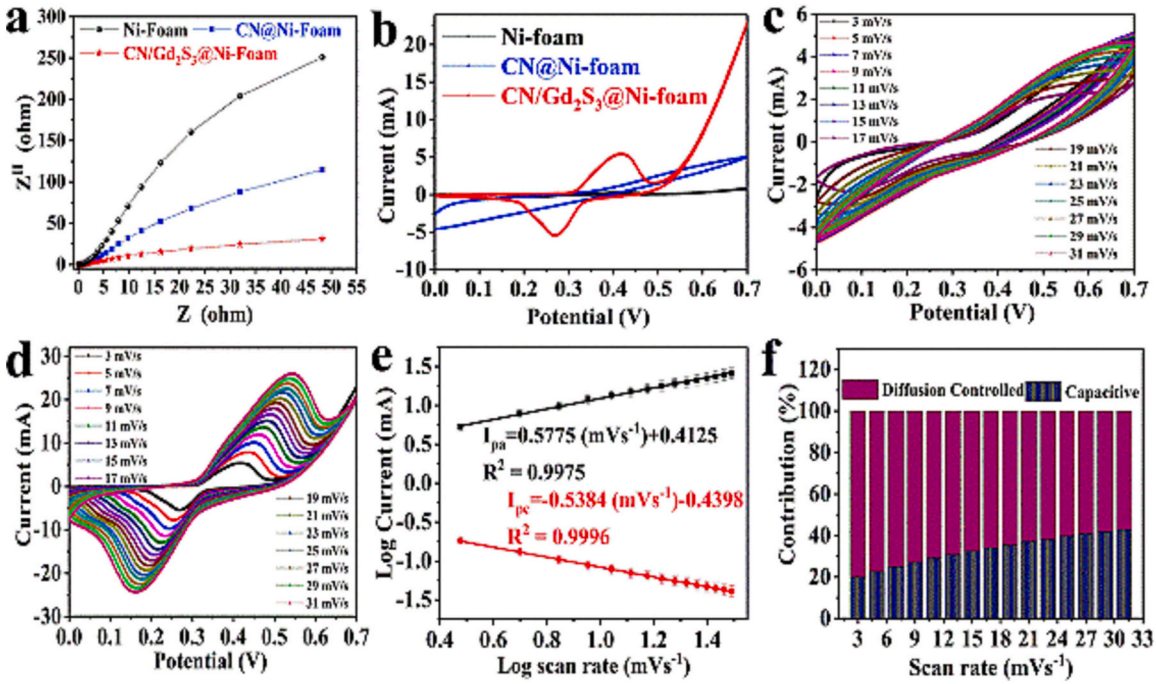

Fig. 3. Nyquist plots and CV curves of bare Ni foam, CN@NF and CN/Gd_2S_3@NF electrode in 2 M KOH (a–b), CN and CN/Gd_2S_3 electrode in 2 M KOH at different scan rates (3–31 mV/s) (c–d), Linear relation between the log scan rate (mV/s) vs log I (mA) of CN/Gd_2S_3 nanocomposite (e) and the relative contributions percentage of the diffusion-controlled and capacitive process for the CN/Gd_2S_3 nanocomposite (f). (For interpretation of the references to color in this figure legend, the reader is referred to the web version of this article.)

at the electrode/electrolyte interface. The electrochemical performance of the different binders and voltage window optimization and this appropriate discussion are provided in Fig. S5 in the ESM. The electrochemical performance of the bare NF (black curve), CN/NF (blue curve), and CN/Gd_2S_3/NF (red curve) was evaluated in a three-electrode cell with a scan rate of 3 mV/s in a 2 M KOH electrolyte, as displayed in Fig. 3b. It is worth noting that the bare NF shows a smaller current in comparison to the CN/NF and CN/Gd_2S_3/NF, indicating that the contribution of the NF toward the capacitance is small under the conditions adopted in the present work. Among them, CN/Gd_2S_3/NF displays a larger current, indicating a higher specific capacitance than the CN/NF electrodes. The enhanced performance of CN/Gd_2S_3/NF might be due to the large surface area promoting ion adsorption sites and the large pore diameter size promoting ion diffusion (as observed by BET results). The CV for CN/NF (blue curve) shows no obvious redox peaks, while CN/Gd_2S_3/NF (red curve) displays redox peaks due to the Faradic reactions arising from the pseudocapacitance effect [32,33].

Furthermore, CV curves of CN and CN/Gd_2S_3 doped NF electrodes were also evaluated at various scan rates of 3–31 mV/s, and the results are displayed in Fig. 3c–d. When the scan rate is increased, both CV curves are well maintained, showing high reversibility. Notably, as the scan rate increases, the pair of redox peaks becomes more prominent, and a slight shift of the redox peaks due to electrochemical polarization is observed [34]. Normally, the overall capacitance of the CN/Gd_2S_3 nanocomposite involves two parts: firstly, diffusion-controlled capacitance; secondly, surface-controlled capacitance, including reversible double-layer capacitance and surface redox pseudocapacitance [1]. The plot of log peak current against log scan rate was generated using the power law relationship described by Eqs. (2) and (3):

$$i = av^b, \tag{2}$$

$$log\ i = log\ a = b\ log\ v \tag{3}$$

in these equations, *a* and *b* represent constants, i is the applied current (mA), v is the scan rate (mV/s). To elaborate, when the 'b' value approximates unity, the peak current exhibits a linear dependency on the scan rate ($i \propto v$). This behavior implies that the material stores charge via a surface redox process. Conversely, when the 'b' value approximates 0.5, the peak current demonstrates a linear relationship with the log scan rate, indicating charge storage through an intercalation redox process, resembling a battery-type storage mechanism, which is associated with diffusion-controlled processes [4]. The regression equations (slope value) and correlation coefficients are given as $I_{pa} = 0.5775$ (mV/s) + 0.4125 and $R^2 = 0.9975$, and $I_{pc} = -0.5384$ (mV/s) − 0.4398 and $R^2 = 0.9996$ is shown in Fig. 3e. The correlation coefficient for redox peaks is almost equal to 1, and the slope value (b) of both anodic and cathodic of CN/Gd_2S_3/NF is 0.57 and − 0.53, which is closer to 0.5, thereby manifesting the unambiguous battery-type storage mechanism of CN/Gd_2S_3 [35]. Furthermore, this Eq. (4) can be used to differentiate this concept,

$$i(V) = KV + K'V^{0.5} \tag{4}$$

If the maximum current is i at a constant voltage (V), then K and K′ are constants. We obtain the slope k by basically plotting the relationship between i and $V^{0.5}$. So, if we calculate the value of k at various voltages at different scan currents, we can plot the capacitance and diffusion control contributions as shown in Fig. 3f, indicating that diffusion control contributes more to the total capacitance. At a scan rate of 3 mV/s, CN/Gd_2S_3 primarily exhibited diffusion-controlled charge storage, with 79.9 % of the total charge being stored within the bulk of the material. Nevertheless, at higher scan rates of 31 mV/s, the contribution of diffusion decreased steadily to 57.09 %. This decline can be attributed to the limited time available for ions to penetrate deep into the material, hindering the efficient facilitation of the redox process within the bulk [36].

The specific capacitance of the synthesized electrode materials was determined using GCD studies of CN (blue curve) and CN/Gd_2S_3 (red curve) in the electrolyte (2 M KOH) at a current density of 1.0 A g^{-1}, and the operating voltage range is 0–0.5 V. In Fig. 4a, the charge/discharge curves in GCD are responsible for the minor primary IR-drop connected to the internal resistance of the material and the consequential nonlinear portion, resulting in pseudocapacitive behavior. The maximum charge/discharge platform in GCD curves is caused by CN/Gd_2S_3, which is capable of high free electron transport during electrochemical reactions, ensuring efficient electron transport. In Fig. 4b–c, the GCD curves of CN/NF and CN/Gd_2S_3/NF electrodes are caused by quasi-reversible faradic reactions at various current densities of 1.0–8.0 A g^{-1}. This result indicates that the charge/discharge time decreases as the current density increases. The battery-like behavior of the GCD curves at the entire current density demonstrates the Faraday result of the electrode constituents. The specific capacitance of CN/NF and CN/Gd_2S_3/NF can be calculated using the relationship [15].

$$C = i \times \Delta t/m \times \Delta v \tag{5}$$

where *i* and Δv represent the applied current and discharge voltage, Δt and *m* denote the discharging time and the mass of the active material on Ni foam respectively. The specific capacitance values at different discharge current densities of 1.0, 2.0, 4.0, 6.0, and 8.0 A g^{-1} are calculated using the above equation to be 590, 463, 371, 264, and 131 F g^{-1} for CN, and 1831, 1522, 1253, 1059, and 799 F g^{-1} for CN/Gd_2S_3 (Fig. 4d–e) in 2 M KOH electrolyte. Meanwhile, CN exhibits low specific capacitance that decreases from 463 to 131 F g^{-1}. Comparing these capacity values highlights the outstanding charge storage capability of the CN/Gd_2S_3/NF electrode as compared to CN/NF. Since the migration of electrolyte ions correlates with higher current densities, the specific capacitance is found to be lower at higher specific current densities [37]. The better electrochemical performance of the specific capacity of the prepared CN/Gd_2S_3/NF is higher than that of other reported metal sulfides and their composite electrodes in the literature, as shown in Table 1 [6,9,38–50].

This demonstrates the good physical contact between CN and Gd_2S_3 material within the composite texture (as probed by FETEM and UHR-FESEM results in Figs. 1b–c & S2) and its complete porous diameter structure (as observed by BET results in Fig. 2f (inset)), serving as vigorous reservoirs for ions and decreasing the ion diffusion path inside the electrodes. Notably, cycle performance tests are a critical factor in assessing electrode materials. For the CN/Gd_2S_3/NF electrode, a continuous GCD test was conducted at current densities of 6.0 A g^{-1}, as displayed in Fig. S7a. The results showed excellent stability for the electrode material throughout the cycle index. The CN/Gd_2S_3/NF electrode was examined for up to 10,000 cycles, and it displayed excellent retention of 98.19 %. This exceptional performance can be attributed to the electrolyte's decomposition at elevated potentials and a superb coulombic efficiency of 98.48 % at 6.0 A g^{-1}, as depicted in Fig. 4f. The electrochemical behavior of the activated carbon (AC) is given in Fig. S6a–b in the ESM. To ensure the practical use of the electrode material CN/Gd_2S_3/NF, an asymmetric supercapacitor (ASC) was made with CN/Gd_2S_3/NF as the positive electrode and AC as the negative electrode, as shown in Fig. 5a. We first compared the electrochemical performance of AC/NF and CN/Gd_2S_3/NF electrodes to establish the optimal operating potential range of −1.0 to 0 V and 0 to 0.7 V in a three-electrode system, as displayed in Fig. 5b. The bare AC electrode exhibits virtually rectangular-shaped CV curves without any distinct redox peaks, displaying its typical double electric layer characteristic [51]. The typical CV curves of CN/Gd_2S_3//AC ASCs are rectangular and show a good electrochemical performance that increases as the scan rate increases from 3 to 39 mV/s, as displayed in Fig. 5c. In Fig. 5c, it can be observed that there is no obvious distortion in each CV curve as the scan rate increases, demonstrating the good rate performance of the ASC device. Moreover, the corresponding GCD analysis was conducted at

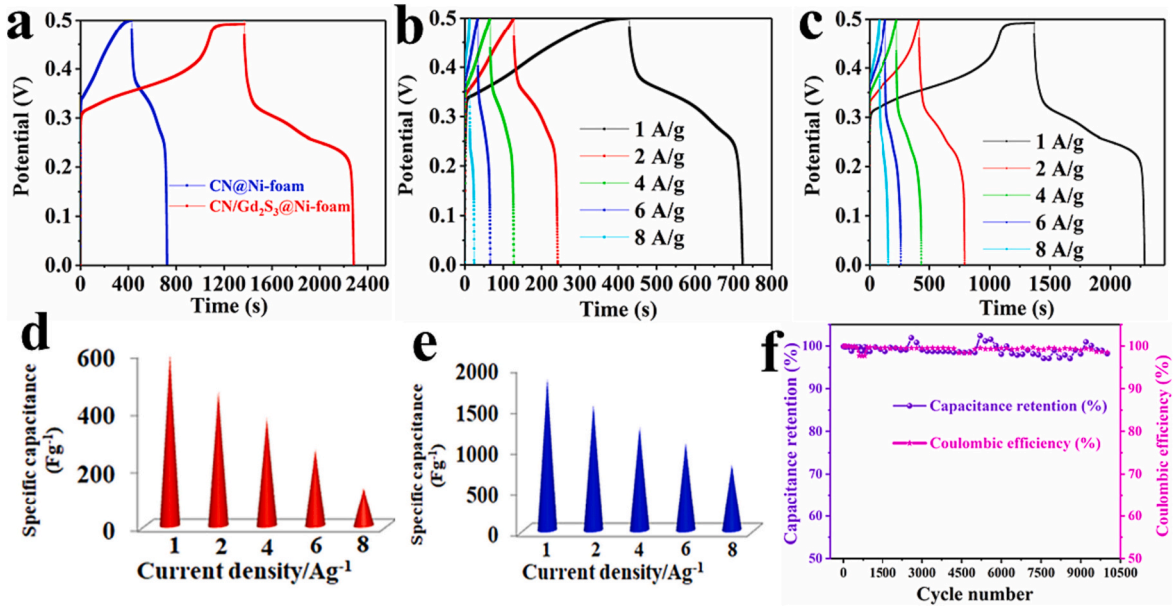

Fig. 4. GCD profiles of CN@Ni foam and CN/Gd_2S_3@Ni foam electrodes in 2 M KOH (a), GCD curves at different current densities (1.0–8.0 A g^{-1}) of CN@Ni foam and CN/Gd_2S_3@Ni foam electrodes in 2 M KOH (b–c), The specific capacitance values at various current densities of CN@Ni foam and CN/Gd_2S_3@Ni foam (d–e) and capacitance retention and coulombic efficiency vs. cycle number of CN/Gd_2S_3@NF (f).

Table 1
Comparative electrochemical SC performance with various metal sulfide based electrode materials.

Electrode materials	Electrolyte/ substrate	Pore diameter (nm)	Specific capacitance (F g^{-1})	Current density (A g^{-1})	Csp retention % up to no. of cycles at a current density	Energy at power density
MoS_2-g-C_3N_4 [6]	1 M Na_2SO_4/NF	–	240.8	1	–	–
$NiCo_2S_4$ NSs/P-g-C_3N_4 [9]	2 M KOH/NF	–	506	1	99 %/5000/at 4 A g^{-1}	16.7 W h kg^{-1} at 200 W kg^{-1}
CoS/NF [38]	2 M KOH/NF	–	395.85	2	97 %/3000 at 20Ag^{-1}	–
3D Ni_3S_2 [39]	1 M KOH/NF	–	470	2	–/2000 cycles at 5 A g^{-1}	88.8 W h kg^{-1} at 480 W kg^{-1}
MnS [40]	1MKOH/SS	–	747	1 mA cm^{-2}	85 %/2000 at 100 mV/s	18.9 W h kg^{-1} at 250 W kg^{-1}
MoS_2/N-doped graphene [41]	1 M KOH/NF	–	245	0.25	91.3 %/1000 at 2 A g^{-1}	–
SnS_2/G [42]	2 M KOH/NF	10	565	1	90 %/3000 at 1Ag^{-1}	23.5 W h kg^{-1} at 880 W kg^{-1}
SS-NiS@3DNF-E-3 [43]	2 M KOH/–	–	694	1	88 %/6700 at 3 A g^{-1}	24.9 W h kg^{-1} at 250.93 W kg^{-1}
NiS_2 [44]	3 M KOH/NF	–	695	1.25	93.4 %/3000 at 1.25 A g^{-1}	15.7 W h kg^{-1} at 254 W kg^{-1}
$NiCo_2S_4$ [45]	1 M KOH/NF	–	2036.5	1	94.3 %/5000 at 100 A g^{-1}	35.6 W h kg^{-1} at 819.5 W kg^{-1}
NiS/PEDOT:PSS-5 [46]	2 M KOH/NF	–	750.6	1.11	91.2 %/3000 at 5.55 A g^{-1}	24.52 W h kg^{-1} at 138.88 W kg^{-1}
Co_3S_4/$CoMo_2S_4$/rGO [47]	3 M KOH/NF	–	1458	1	97 %/2000 cycles	33.1 W h kg^{-1} at 850 W kg^{-1}
SnS_2/g-C_3N_4 [48]	3 M KOH/–	–	552	0.5	95 %/15000 cycles	1.6 W h kg^{-1} at 3050 W kg^{-1}
$CuCo_2S_4$ [49]	2 M KOH/NF	5	752	2	98.1 %/5000 at 3 A g^{-1}	–
$NiCo_2S_4$@MnO_2 [50]	6 M KOH/nickel foil	–	1337.8	2	82 %/2000 at 2 A g^{-1}	–
CN/Gd_2S_3 [present work]	**2 M KOH/NF**	**11.36**	**1831**	**1**	**98.5 %/5000 at 6 A g^{-1}**	**70.95 W h kg^{-1} at 250 W kg^{-1}**

different current densities ranging from 1.0 to 8.0 A g^{-1} within a fixed potential range of 0 to 1.8 V. Additionally, small IR droplets are shown in Fig. 5d, which represent simple ion exchange channels through electrolyte ions to disrupt and de-intercalate electroactive sites within the pore [39]. The obtained GCD curve contains two regions representing the following mechanisms: (i) a plateau region due to the deep penetration of electrolyte ions, and (ii) a relatively quick potential decay corresponding to the EDLC mechanism [1,11,52]. The specific capacitances of the ASC were calculated at different discharge current loads of 1.0, 2.0, 4.0, 6.0, and 8.0 A g^{-1}, resulting in values of 157.6, 111.1, 93.5, 45.2, and 19.1 F g^{-1}, as shown in Fig. 5e.

Furthermore, long cycle life is significant for any ASC electrode material intended for commercial use, and the GCD analysis is performed to estimate the cycle performance of the ASC electrode. The maximum capacitance retention strategy of the synthesized ASC electrode is found to be 86.8 % after 5000 cycles at 8.0 A g^{-1}, and it exhibits an excellent coulombic efficiency of 95.1 %, as displayed in Fig. 5f. A continuous GCD curve for the CN/Gd_2S_3//AC electrode was examined at

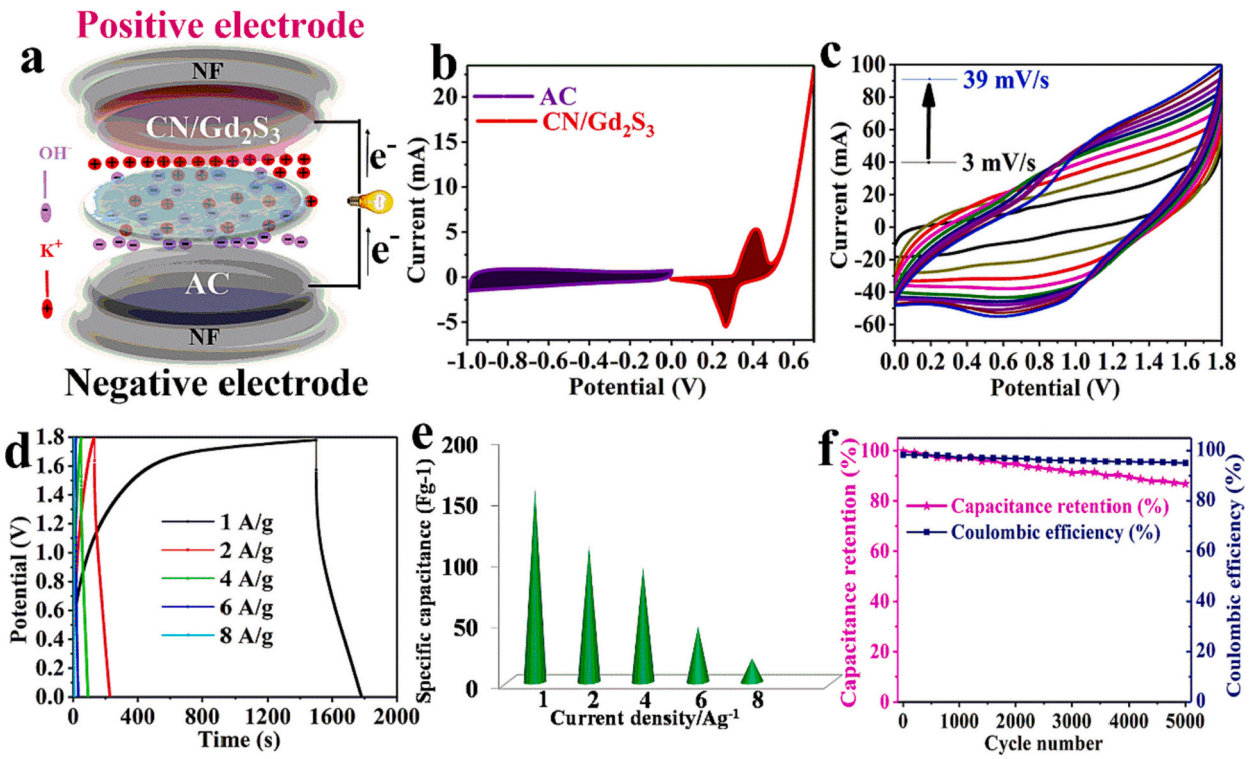

Fig. 5. Schematic illustration of a solid-state SC composed of an AC@NF and CN/Gd_2S_3@NF electrode (a), CV of AC@NF and CN/Gd_2S_3@Ni foam electrode at 3 mV/s (b), CV plots (c) GCD plots of the CN/Gd_2S_3//AC solid-state SC (d), specific capacitance vs current density function of CN/Gd_2S_3//AC (e) and cycling stability and Coulombic efficiency of CN/Gd_2S_3//AC at 8.0 A g^{-1} (f).

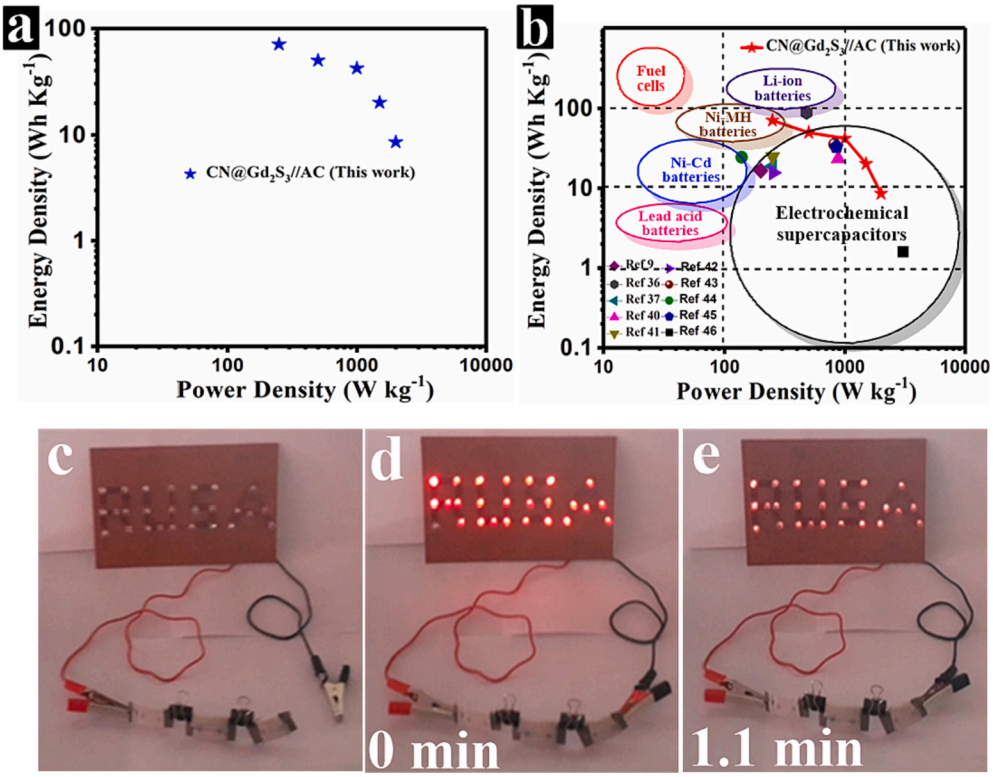

Fig. 6. Ragone plot of the CN/Gd_2S_3//AC (a) and a comparison with other reported solid-state SC based on metal sulfides (b) and optical images of ASC devices connected in series to powered 26 red LEDs lit up by three as-fabricated devices in series (c–e). (For interpretation of the references to color in this figure legend, the reader is referred to the web version of this article.)

a current load of 8.0 A g^{-1}, as displayed in Fig. S7b. The UHR-SEM images of CN/Gd_2S_3 after 5000 are given in Fig. S7c–d in the ESM. The cycle index for the electrode material indicated excellent stability. This result suggests that the greater efficiency is attributed to the porous nature of CN/Gd_2S_3//AC, which leads to higher capacity retention and superior cycle stability.

Also, the energy density (E) and power density (P) of the CN/Gd_2S_3//AC ASC device are evaluated using the equation below [40].

$$E = \mathrm{C} \times \Delta \mathrm{V}^2 / 7.2 \ \left(\mathrm{W\ h\ kg^{-1}}\right) \quad (6)$$

$$P = \mathrm{E} / \Delta \mathrm{t} \ \left(\mathrm{kW\ kg^{-1}}\right) \quad (7)$$

where, C is the specific capacitance (F g^{-1}) of the ASC calculated by the total mass of active materials, ΔV is the operation potential voltage window of the cell and Δt denotes the discharging time (s).

In addition, the energy and power density of the CN/Gd_2S_3//AC ASC were evaluated using the above Eqs. (6) & (7). As can be seen in the Ragone plot (Fig. 6a), the supreme energy density for the CN/Gd_2S_3//AC ASC is 70.95 W h kg^{-1} at a power density of 0.250 kW kg^{-1} (250 W kg^{-1}), and the highest power density of 1.99 kW kg^{-1} (1999 W kg^{-1}) can be sustained at an energy density of 8.59 W h kg^{-1}. Furthermore, the energy and power density of the CN/Gd_2S_3//AC ASC is greater than that of $NiCo_2S_4$ NSs/P-g-C_3N_4 [9], 3D Ni_3S_2 [39], MnS [40], SnS_2/G [42], SS-NiS@3DNF-E-3 [43], NiS_2 [44], $NiCo_2S_4$ nanopetals [45], NiS/PEDOT:PSS-5 [46], Co_2S_4/$CoMo_2S_4$/rGO [47], SnS_2/g-C_3N_4 [48], as displayed in Fig. 6b. As shown in Table 1, the CN/Gd_2S_3//AC electrodes offer high energy and power density and reasonable rate retention. These investigational results indicate that the synthesized CN/Gd_2S_3 electrode possesses excellent electrochemical properties, making it one of the most attractive candidates for energy-related studies. The real-life practical application of the CN/Gd_2S_3//AC supercapacitor device was demonstrated by powering twenty-six red LEDs (each rated at 2.7 V) for 1.1 min without any interruption (Fig. 6c–e). These results indicate that the CN/Gd_2S_3//AC ASC holds great promise for practical applications. The outstanding energy storage capability of the ASC device suggests its viability for use in electronic devices.

5. Conclusion

In summary, a new nanocomposite CN/Gd_2S_3 was successfully prepared via a one-step in situ thermal reduction method, and the synthesized material acted as active electrodes for supercapacitors (SC). The as-synthesized CN/Gd_2S_3@NF electrode exhibited a higher specific capacitance of 1831 F g^{-1} at 1.0 A g^{-1}. Moreover, a long cycle life with capacitance retention of 98.5 % was achieved after 5000 cycles at 6.0 A g^{-1}. Based on this, the synthesized CN/Gd_2S_3@NF was utilized as the positive electrode, while AC was employed as the negative electrode, forming an asymmetric supercapacitor (CN/Gd_2S_3//AC, ASC). The synthesized ASC offers a high capacitance of 157.6 F g^{-1} at a current density of 1.0 A g^{-1} and an excellent energy density of 70.95 W h kg^{-1} at a power density of 0.250 kW kg^{-1} (250 W kg^{-1}). The excellent electrochemical performance is attributed to the synergy and strategic integration of CN and Gd_2S_3, which results in a high pore diameter size and enhanced electron transfer acceleration to increase reaction kinetics. Moreover, the fabricated ASC electrode displayed long-cycle stability with a specific capacitance retention rate of 86.8 % over 5000 cycles at 8.0 A g^{-1} and achieved an excellent coulombic efficiency of 95.1 %. Furthermore, the outstanding electrochemical performance of this device (CN/Gd_2S_3//AC) was demonstrated by powering twenty-six light-emitting diodes (LEDs), which further confirm its viability as a candidate for high-energy ASC. The discovery of this ASC holds promise as a template for next-generation energy storage and conversion applications.

CRediT authorship contribution statement

Ponnaiah Sathish Kumar: Conceptualization, Methodology, Investigation, Data curation, Visualization, Writing – original draft, Writing – review & editing. **Yuho Min:** Investigation, Data curation. **Dong Choon Hyun:** Investigation, Data curation. **Ji-Hyuk Choi:** Conceptualization, Investigation, Data curation, Writing – review & editing. **Sungwon Lee:** Conceptualization, Investigation, Data curation, Visualization, Funding acquisition, Project administration, Supervision, Writing – original draft, Writing – review & editing.

Declaration of competing interest

The authors declare that they have no known competing financial interests or personal relationships that could have appeared to influence the work reported in this paper.

Data availability

Data will be made available on request.

Acknowledgments

We would like to express our deepest gratitude to the National Research Foundation of Korea for its research grant support (grant Nos. 2018R1A5A1025511, 2022R1A2C100829211(22-6806), RS-2023-00249905), the Basic Research Project (Grant Number: 23-3810) of the Korea Institute of Geoscience and Mineral Resources funded by the Ministry of Science and ICT of Korea and the BK21 FOUR (Fostering Outstanding Universities for Research) funded by the Ministry of Education (MOE, Korea).

Appendix A. Supplementary data

Supplementary data to this article can be found online at https://doi.org/10.1016/j.est.2023.109385.

References

[1] S. Ding, J. An, Y. Gao, D. Ding, X. Lu, L. Zhao, Electrochemical performance of all-solid-state asymmetric supercapacitors based on Cu/Ni-Co(OH)$_2$/Co_4S_3 self-supported electrodes, Chem. Eng. J. 453 (2023), 139714.
[2] X. Xing, X. Wang, W. Wang, C. Yang, H. Wang, Hierarchically porous N-doped carbon nanosheet aerogel cathodes for Zn-ion hybrid supercapacitors with super high energy density, J. Energy Storage 68 (2023), 107822.
[3] Y. Peng, W. Yuan, X. Liu, P. Xie, F. Yang, H. Zhao, D. Lu, Y. Yin, Z. Wu, All-in-one integration of polyaniline-polyvinyl alcohol electrode/electrolyte interface for tailorable solid-state supercapacitors, J. Energy Storage 61 (2023), 106701.
[4] H.R. Inta, H.V.S.R.M. Koppisetti, S. Ghosh, A. Roy, V. Mahalingam, J. Zhang, J. Feng, Y. Tian, Y. Wu, X. Liu, Q. He, Ni_3Se_4 nanostructure as a battery-type positive electrode for hybrid capacitors, Chem. Electro. Chem. 10 (2) (2023), e202201041.
[5] A.A. Hor, N. Yadav, S.A. Hashmi, Enhanced energy density quasi-solid-state supercapacitor based on an ionic liquid incorporated aqueous gel polymer electrolyte with a redox-additive trimethyl sulfoxonium iodide, J. Energy Storage 64 (2023), 107227.
[6] S.A. Ansari, M.H. Cho, Simple and large scale construction of MoS_2-g-C_3N_4 heterostructures using mechanochemistry for high performance electrochemical supercapacitor and visible light photocatalytic applications, Sci. Rep. 7 (2017) 43055.
[7] K.C. Devarayapalli, K. Lee, H.-B. Do, N.N. Dang, K. Yoo, J. Shim, S.V. Prabhakar Vattikuti, Mesostructured g-C_3N_4 nanosheets interconnected with V_2O_5 nanobelts as electrode for coin-cell-type-asymmetric supercapacitor device, Mater. Today Energy 21 (2021), 100699.
[8] K.G. Subhash, M.D. Benoy, J. Duraimurugan, S. Prabhu, R. Siranjeevi, R. Ramesh, G. Suresh Kumar, M. Shkir, Synergistic effect of NiS/g-C_3N_4 nanocomposite for high-performance asymmetric supercapacitors, Inorg. Chem. Commun. 142 (2022), 109719.
[9] Z. Li, L. Wu, L. Wang, A. Gu, Q. Zhou, Nickel cobalt sulfide nanosheets uniformly anchored on porous graphitic carbon nitride for supercapacitors with high cycling performance, Electrochim. Acta 231 (2017) 617–625.
[10] X. Rui, H. Tan, Q. Yan, Nanostructured metal sulfides for energy storage, Nanoscale 6 (2014) 9889–9924.

[11] S.K. Ponnaiah, P. Prakash, A new high-performance supercapacitor electrode of strategically integrated cerium vanadium oxide and polypyrrole nanocomposite, Int. J. Hydrog. Energy 46 (37) (2021) 19323.

[12] H.M. Shiri, A. Ehsani, Pulse electrosynthesis of novel wormlike gadolinium oxide nanostructure and its nanocomposite with conjugated electroactive polymer as a hybrid and high efficient electrode material for energy storage device, J. Colloid Interface Sci. 484 (2016) 70–76.

[13] V. Mariyappan, M. Keerthi, S.M. Chen, Highly selective electrochemical sensor based on gadolinium sulfide rod-embedded RGO for the sensing of carbofuran, J. Agric. Food Chem. 69 (2021) 2679–2688.

[14] K. Yogesh Kumar, M.K. Prashanth, L. Parashuram, B. Palanivel, F.A. Alharti, B. H. Jeon, M.S. Raghu, Gadolinium sesquisulfide anchored N-doped reduced graphene oxide for sensitive detection and degradation of carbendazim, Chemosphere 296 (2022), 134030.

[15] Y. Zhao, Y. Luo, B. Sun, T. Li, S. Han, Z. Dong, H. Lin, Rational construction of reduced $NiCo_2S_4$@$CuCo_2S_4$ composites with sulfur vacancies as high-performance supercapacitor electrode for enhancing electrochemical energy storage, Compos. Part B 243 (2022), 110088.

[16] S.S. Pujari, S.A. Kadam, Y.-R. Ma, S.B. Jadhav, S.S. Kumbhar, S.B. Bhosale, V. V. Patil, J.L. Gunjakar, C.D. Lokhande, U.M. Patil, A binder-free facile synthetic approach for amorphous, hydrous nickel copper phosphate thin film electrode preparation and its application as a highly stable cathode for hybrid asymmetric supercapacitors, Sustain. Energy Fuels 6 (24) (2022) 5608–5620.

[17] F. Markoulidis, A. Dawe, C. Lekakou, Electrochemical double-layer capacitors with lithium-ion electrolyte and electrode coatings with PEDOT:PSS binder, J. Appl. Electrochem. 51 (2021) 373–385.

[18] M. Yoonessi, A. Borenstein, M.F. El-Kady, C.L. Turner, H. Wang, A.Z. Stieg, L. Pilon, Hybrid transparent PEDOT:PSS molybdenum oxide battery-like supercapacitors, ACS Appl. Energy Mater. 2 (2019) 4629–4639.

[19] J.-H. Choi, C. Lee, S. Cho, G.D. Moon, B.-su Kim, H. Chang, H.D. Jang, High capacitance and energy density supercapacitor based on biomass-derived activated carbons with reduced graphene oxide binder, Carbon 132 (2018) 16–24.

[20] J.-H. Choi, Y. Kim, B.-su Kim, Multifunctional role of reduced graphene oxide binder for high performance supercapacitor with commercial-level mass loading, J. Power Sources 454 (2020), 227917.

[21] J. Balasubramanian, S.K. Ponnaiah, P. Periakaruppan, D. Kamaraj, Accelerated photodeterioration of class I toxic monocrotophos in the presence of one-pot constructed Ag_3PO_4/polyaniline@g-C_3N_4 nanocomposite: efficacy in light harvesting, Environ. Sci. Pollut. Res. 27 (2020) 2328–2339.

[22] S.K. Ponnaiah, P. Prakash, J. Balasubramanian, Effective and reliable platform for nonenzymatic nanomolar-range quinol detection in water samples using ceria doped polypyrrole nanocomposite embedded on graphitic carbon nitride nanosheets, Chemosphere 271 (2021), 129533.

[23] S.K. Ponnaiah, P. Prakash, S. Muthupandian, Ultrasonic energy-assisted in-situ synthesis of Ru^0/PANI/g-C_3N_4 nanocomposite: application for picomolar-level electrochemical detection of endocrine disruptor (Bisphenol-A) in humans and animals, Ultrason. Sonochem. 58 (2019), 104629.

[24] B. Dong, M. Li, S. Chen, D. Ding, W. Wei, G. Gao, S. Ding, Formation of g-C_3N_4@Ni$(OH)_2$ honeycomb nanostructure and asymmetric supercapacitor with high energy and power density, ACS Appl. Mater. Interfaces 9 (2017) 17890–17896.

[25] Q. Yu, Q. Xu, H. Li, K. Yang, X. Li, Effects of heat treatment on the structure and photocatalytic activity of polymer carbon nitride, J. Mater. Sci. 54 (2019) 14599–14608.

[26] V. Alman, K. Singh, T. Bhat, A. Sheikh, S. Gokhale, Sunlight assisted improved photocatalytic degradation of rhodamine B using Pd-loaded g-C_3N_4/WO_3 nanocomposite, Appl. Phys. A Mater. Sci. Process. 126 (2020) 724.

[27] P. Matheswaran, P. Karuppiah, S.M. Chen, P. Thangavelu, B. Ganapathi, Fabrication of g-C_3N_4 nanomesh-anchored amorphous $NiCoP_2O_7$: tuned cycling life and the dynamic behavior of a hybrid capacitor, ACS Omega 3 (2018) 18694–18704.

[28] S. Alagar, S. Kumari, D. Upreti, V. Bagchi Aashi, High-performance Mg-ion supercapacitor designed with a N-doped graphene wrapped $CoMn_2O_4$ and porous carbon spheres, Energy Fuel 36 (23) (2022) 14442–14452.

[29] N.F. Sylla, N.M. Ndiaye, B.D. Ngom, D. Momodu, M.J. Madito, B.K. Mutuma, N. Manyala, Effect of porosity enhancing agents on the electrochemical performance of high-energy ultracapacitor electrodes derived from peanut shell waste, Sci. Rep. 9 (2019) 13673.

[30] C. Zhong, Y. Deng, W. Hu, J. Qiao, L. Zhang, J. Zhang, A review of electrolyte materials and compositions for electrochemical supercapacitors, Chem. Soc. Rev. 44 (2015) 7484–7539.

[31] G.M.V. Dias, J.C. Bernardes, B.N. Wesling, D. Müller, L.S. Marques, C.R. Rambo, Preparation and electrochemical capacitance of high surface area TiO_2–RuO_2 aerogels, Open Ceram. 8 (2021), 100196.

[32] J. Kavil, P.M. Anjana, P. Periyat, R.B. Rakhi, One-pot synthesis of g-C_3N_4/MnO_2 and g-C_3N_4/SnO_2 hybrid nanocomposites for supercapacitor applications, Sustain. Energy Fuels 2 (2018) 2244–2251.

[33] H. Tomiyasu, H. Shikata, K. Takao, N. Asanuma, S. Taruta, Y.Y. Park, An aqueous electrolyte of the widest potential window and its superior capability for capacitors, Sci. Rep. 7 (2017) 45048.

[34] K.S. Ranjith, D.R. Kumar, S.M. Ghoreishian, Y.S. Huh, Y.-K. Han, R.T.R. Kumar, A radially controlled ZnS interlayer on ultra-long ZnO–Gd_2S_3 core–shell nanorod arrays for promoting the visible photocatalytic degradation of antibiotics, Nanoscale 12 (2020) 14047–14060.

[35] H. Kim, M.-Y. Cho, M.-H. Kim, K.-Y. Park, H. Gwon, Y. Lee, K.C. Roh, K. Kang, A novel high-energy hybrid supercapacitor with an anatase TiO_2–reduced graphene oxide anode and an activated carbon cathode, Adv. Energy Mater. 3 (2013) 1500–1506.

[36] M. Isacfranklin, R. Yuvakkumar, G. Ravi, S.I. Hong, F. Shini, M. Thambidurai, C. Dang, D. Velauthapillai, Marigold flower like structured Cu_2NiSnS_4 electrode for high energy asymmetric solid state supercapacitors, Sci. Rep. 10 (2020) 19198.

[37] W. Zhao, J. Yi, P. He, H. Zhou, Solid-state electrolytes for lithium-ion batteries: fundamentals, challenges and perspectives, Electrochem. Energy Rev. 2 (2019) 574–605.

[38] K.D. Ikkurthi, S.S. Rao, M. Jagadeesh, A.E. Reddy, T. Anitha, H.J. Kim, Synthesis of nanostructured metal sulfides via a hydrothermal method and their use as an electrode material for supercapacitors, New J. Chem. 42 (2018) 19183–19192.

[39] Z. Zhang, Z. Huang, L. Ren, Y. Shen, X. Qi, J. Zhong, One-pot synthesis of hierarchically nanostructured Ni_3S_2 dendrites as active materials for supercapacitors, Electrochim. Acta 149 (2014) 316–323.

[40] R.B. Pujari, A.C. Lokhande, A.A. Yadav, J.H. Kim, C.D. Lokhande, Synthesis of MnS microfibers for high performance flexible supercapacitors, Mater. Des. 108 (2016) 510–517.

[41] B. Xie, Y. Chen, M. Yu, T. Sun, L. Lu, T. Xie, Y. Zhang, Y. Wu, Hydrothermal synthesis of layered molybdenum sulfide/N-doped graphene hybrid with enhanced supercapacitor performance, Carbon 99 (2016) 35–42.

[42] S.P. Lonkar, V.V. Pillai, S.P. Patole, S.M. Alhassan, Scalable in situ synthesis of 2D−2D-type graphene-wrapped SnS_2 nanohybrids for enhanced supercapacitor and electrocatalytic applications, ACS Appl. Energy Mater. 3 (2020) 4995–5005.

[43] B.T. Al-Abawi, N. Parveen, S.A. Ansari, Controllable synthesis of sphere-shaped interconnected interlinked binder-freenickel sulfide@nickel foam for high-performance supercapacitor applications, Sci. Rep. 12 (2022) 14413.

[44] H. Pang, C. Wei, X. Li, G. Li, Y. Ma, S. Li, J. Chen, J. Zhang, Microwave-assisted synthesis of NiS_2 nanostructures for supercapacitors and cocatalytic enhancing photocatalytic H_2 production, Sci. Rep. 4 (2014) 3577.

[45] Y. Wen, S. Peng, Z. Wang, J. Hao, T. Qin, S. Lu, J. Zhang, D. He, X. Fan, G. Cao, Facile synthesis of ultrathin $NiCo_2S_4$ nano-petals inspired by blooming buds for high-performance supercapacitors, J. Mater. Chem. A 5 (2017) 7144–7152.

[46] S.S. Rao, D. Punnoose, J.H. Bae, I.K. Durga, C.V. Thulasi-Varma, B. Naresh, A. Subramanian, V. Raman, H.J. Kim, Preparation and electrochemical performances of NiS with PEDOT:PSS chrysanthemum petal like nanostructure for high performance supercapacitors, Electrochim. Acta 254 (2017) 269–279.

[47] X. Yang, H. Sun, P. Zan, L. Zhao, J. Lian, Growth of vertically aligned Co_3S_4/$CoMo_2S_4$ ultrathin nanosheets on reduced graphene oxide as a high-performance supercapacitor electrode, J. Mater. Chem. A 4 (2016) 18857–18867.

[48] Y. Xu, Y. Zhou, J. Guo, S. Zhang, Y. Lu, Preparation of SnS_2/g-C_3N_4 composite as the electrode material for supercapacitor, J. Alloys Compd. 806 (2019) 343–349.

[49] Y. Zhu, X. Ji, H. Chen, L. Xi, W. Gong, Y. Liu, The investigation of the electrochemically supercapacitive performances of mesoporous $CuCo_2S_4$, RSC Adv. 6 (2016) 84236–84241.

[50] J. Yang, M. Ma, C. Sun, Y. Zhang, W. Huang, X. Dong, Hybrid $NiCo_2S_4$@MnO_2 heterostructures for high performance supercapacitor electrodes, J. Mater. Chem. A 3 (2015) 1258–1264.

[51] X. Deng, J. Li, Z. Shan, J. Sha, L. Ma, N. Zhao, A N, O co-doped hierarchical carbon cathode for high-performance Zn-ion hybrid supercapacitors with enhanced pseudocapacitance, J. Mater. Chem. A 8 (2020) 11617–11625.

[52] M. Priyadharshini, M. Sandhiya, M. Sathish, T. Pazhanivel, G. Mani, A. A. Alothman, K.N. Alqahtani, Surfactant-dependant self organisation of nickel pyrophosphate for electrochemical supercapacitors, J. Mater. Sci. Mater. Electron. 33 (2022) 9269–9276.